Open access • Posted Content • DOI:10.1101/2021.05.12.443573

microRNA-138 controls hippocampal interneuron function and short-term memory

Daswani R, Gilardi C, Michael Soutschek, Weiss K ...+6 more authors

Institutions: École Polytechnique Fédérale de Lausanne, University of Marburg, Heidelberg University

Published on: 13 May 2021 - bioRxiv (ETH Zurich)

Topics: Neurotransmission, Inhibitory postsynaptic potential, Excitatory postsynaptic potential and Hippocampal formation

microRNA-138 controls hippocampal interneuron function and short-term memory

Daswani, R.[1], Gilardi, C.[1], Soutschek, M.[1], Weiss, K.[2], Bicker, S.[1], Fiore, R.[1], Dieterich, C.[3], Germain, P.L.[1], Winterer, J*[1], Schratt, G*[1].

[1]Lab of Systems Neuroscience, Institute for Neuroscience, Department of Health Science and Technology, Swiss Federal Institute of Technology ETH, 8057 Zurich, Switzerland

[2]Institute for Physiological Chemistry, Biochemical-Pharmacological Center Marburg, Philipps-University of Marburg, 35032 Marburg, Germany

[3]Section of Bioinformatics and Systems Cardiology, Department of Internal Medicine III and Klaus Tschira Institute for Integrative Computational Cardiology, University of Heidelberg, Germany

*co-corresponding authors: jochen.winterer@hest.ethz.ch; gerhard.schratt@hest.ethz.ch

Keywords: microRNA, interneuron, inhibitory synapse, working memory, schizophrenia

Summary

A tightly regulated balance between excitatory and inhibitory (E/I) synaptic transmission is critical for neural circuit assembly and function. microRNAs control excitatory neuron function, but their role in inhibitory interneurons is unknown. Here, we show that miR-138-5p regulates the expression of presynaptic genes in hippocampal parvalbumin-expressing inhibitory interneurons to control short-term memory. Our finding suggests a critical role for miR-138-5p in disorders of impaired E/I balance, such as autism and schizophrenia.

Introduction

The function of neural circuits critically depends on a fine-tuned balance between synaptic excitation and inhibition, the so-called “excitatory-inhibitory (E-I) balance” (Rubenstein and Merzenich, 2003). In the rodent hippocampus, microcircuits of excitatory pyramidal neurons and local inhibitory interneurons provide an extensively studied model highlighting the functional relevance of E-I balance in the context of information processing, learning and memory (Booker and Vida, 2018; Markram et al., 2004; Pelkey et al., 2017). Among the different interneuron classes, fast-spiking parvalbumin (PV) expressing interneurons play a particularly prominent role in controlling pyramidal neuron output to drive appropriate behavioral responses (Murray et al., 2011; Rico and Marin, 2011). Disruptions in E-I balance associated with PV interneuron dysfunction have been implicated in epilepsy, autism-spectrum disorders (ASD) and schizophrenia (Del Pino et al., 2018; Sohal and Rubenstein, 2019).

microRNAs (miRNAs), short non-coding RNAs which act as negative regulators of mRNA translation and stability(Bartel, 2018), control excitatory neuron development, function and plasticity (McNeill and Van Vactor, 2012; Schratt, 2009). Likewise, miRNAs are substantially expressed in inhibitory γ-aminobutyric acid (GABA)ergic interneurons (He et al., 2012). The complete lack of miRNAs reduces the number of cortical interneurons (Tuncdemir et al., 2015) while the absence of miRNAs in interneurons expressing vasoactive intestinal peptide (VIP) leads to cortical circuit dysfunction (Qiu et al., 2020). However, the role of specific miRNAs in inhibitory interneurons in the context of higher cognitive function is completely elusive.

Results

We previously identified the brain-enriched miR-138-5p as an important regulator of excitatory synapse function in hippocampal pyramidal neurons(Siegel et al., 2009). To study the role of miR-138-5p on a behavioral level, we generated mice with a conditional ROSA26 transgene (138-floxed) which allows expression of a miR-138-5p inactivating sponge transcript harboring 6 imperfect miR-138-5p binding sites (6x-miR-138sponge) upon Cre-recombinase expression. Sponge transcripts sequester endogenous miRNA, thereby leading to miRNA inactivation and the de-repression of cognate target genes(Ebert and Sharp, 2010).

We activated 138-sponge expression at embryonic stage by crossing 138-floxed mice to the ubiquitous Cre-driver line CMV-Cre (138-sponge^{ub}, **Fig. 1a**) after validating specificity and efficiency of 6x-miR-138-sponge in primary rat hippocampal neurons (**suppl. Fig. 1a, b, c**).138-floxed mice without CMV transgene served as control line. lacZ staining revealed highly penetrant expression of 6x-miR-138 sponge in the brain of 138-sponge^{ub} mice (**suppl. Fig. 1d**). To test for the degree of miR-138-5p inhibition *in vivo* we made use of a dual fluorescence miR-138 sensor virus which we injected into the hippocampus of 138-sponge^{ub} mice. Analysis disclosed a significant increase in intensity of the GFP signal in neurons with 6x-miR-138-sponge expression compared to controls, indicative of an efficient sequestering of endogenous miR-138-5p by our sponge construct (**Fig. 1b**).

We next assessed cognitive abilities of 138-sponge^{ub} mice using behavioral testing. Locomotion in the home cage was similar between 138-sponge^{ub} and control mice, ruling out severe developmental motor impairments as a potential confound (**suppl. Fig.1e**). In the Y-maze test, no genotype-dependent differences in spontaneous alternations were observed, suggesting that exploratory behavior was not affected by miR138-5p inactivation (**suppl. Fig. 1f**). In contrast, 138-sponge^{ub} mice displayed a significant impairment in novelty preference (**Fig. 1c**), indicating a loss of spatial short-term memory. In the novel object recognition (NOR) task, 138-sponge^{ub} mice were unable to discriminate the novel from the familiar object (**Fig. 1d**), thereby corroborating the observed short-term memory deficit. In contrast, associative long-term memory, as assessed by classical fear conditioning (**Fig. 1e**), as well as anxiety-related behavior (open field, EPM), was not affected by miR-138-5p inhibition (**suppl.**

Fig. 1g, h). Thus, ubiquitous miR-138-5p inhibition leads to a specific short-term memory deficit.

We went on to test whether short-term memory impairments in 138-sponge^{ub} mice were associated with alterations in synaptic transmission in hippocampal area CA1 and recorded miniature excitatory postsynaptic currents (mEPSCs) in CA1 pyramidal neurons. Amplitude and frequency of mEPSCs were indistinguishable between 138-sponge^{ub} and control slices (**Fig. 1f**, **suppl. Fig. 1i, j**). Likewise, we did not detect any significant alterations in dendritic spine morphology in these neurons using Golgi staining (**Fig. 1g**). Finally, we did not observe differences in paired-pulse ratio (PPR), which negatively correlates with presynaptic release probability (**suppl. Fig. 1k**), suggesting that excitatory synaptic transmission at the Schaffer collateral CA1 pyramidal cell synapse was not affected by miR-138-5p inhibition.

To identify miR-138-5p target mRNAs and to obtain further insight into the biological function of miR-138-5p regulated genes, we performed polyA-RNA sequencing with total RNA isolated from hippocampal tissue. Differential gene expression analysis recovered a total of 322 differentially expressed genes (DEG; 257 upregulated, 65 downregulated) (FDR<0.05; **Fig. 2a**). The presence of miR-138-5p binding sites correlated with increased transcript levels compared with 138-floxed mice (**Fig. 2b**). miR-138-5p 7-mer 1a, and to a lesser extent 7mer-m8 and 8mer sites, predicted significant de-repression (**suppl. Fig. 2a**). In total, 56 (21%) of the upregulated, but only 6 (8%) of the downregulated genes harbor miR-138-5p binding sites within their 3'UTR. Together, this data demonstrates that many of the observed upregulated genes are a direct consequence of miR-138-5p inhibition.

Gene ontology (GO) term analysis on DEGs from the RNA-seq analysis (**Fig. 2c**; **suppl. Fig. 2b**) revealed that many GO terms associated with synaptic function are strongly over-represented in genes upregulated in the hippocampus of 138-sponge^{ub} mice. In order to specify the origin for the observed gene expression changes, we compared DEGs to single cell RNA-seq data from different cell types present in the hippocampus(Zeisel et al., 2018) (**Fig. 2d**). Surprisingly, we found that those genes which were significantly upregulated in 138-sponge^{ub} mice are strongly enriched in inhibitory GABAergic interneurons. This finding is in line with the observation that excitatory synaptic transmission in hippocampal CA1 was not affected by miR-138-5p inactivation (**Fig. 1f**, **suppl. Fig. 1i, j, k**). Accordingly, many of the upregulated miR-138-5p targets showed a strong expression signal in different classes of inhibitory

interneurons (**suppl. Fig. 2c**). Taken together, miR-138-5p inactivation leads to a preferential upregulation of synaptic genes which are predominantly expressed in inhibitory interneurons.

Next, we performed single-molecule miRNA FISH in cultured rat hippocampal neurons to visualize miR-138-5p expression at subcellular resolution. This analysis revealed strong expression of miR-138-5p in both Camk2a-positive excitatory and Erbb4-positive inhibitory hippocampal neurons (**Fig. 2e**). Erbb4-positive cells express Gad65, but not Camk2a, confirming their GABAergic phenotype (**Fig. 2e**). In contrast, miR-138-5p expression was undetectable in GFAP-positive glial cells (**suppl. Fig. 2d**). Thus, miR-138-5p is robustly expressed in inhibitory interneurons, consistent with a previously unrecognized function in these cells.

We went on to validate miR-138-5p dependent regulation of predicted interneuron-enriched target genes, focusing on Erbb4 (Erb-B2 receptor tyrosine kinase 4) and the presynaptic release machinery constituent Rims3 (Regulating synaptic membrane exocytosis 3) (**suppl. Fig. 2e**). Using qPCR, we observed a significant upregulation of both Erbb4 and Rims3 mRNA levels in the hippocampus of 138-sponge^{ub} compared to 138-floxed mice, thereby validating our results from RNA-seq (**Fig. 2f**). In luciferase reporter gene assays, transfection of miR-138-5p significantly reduced the expression of both Erbb4 and Rims3 3'UTR constructs containing a wild-type, but not mutant miR-138-5p binding site (**Fig. 2g, h**), rendering Erbb4 and Rims3 as direct miR-138-5p targets.

To elaborate on the functional role of miR-138-5p in inhibitory interneurons, we generated 138-sponge^{PV} mice by crossing 138-floxed mice to PV-Cre mice (**Fig. 3a**). In 138-sponge^{PV} mice, the 6x-miR-138-sponge transcript is selectively expressed in the majority (about 90%) of PV-expressing inhibitory interneurons (PV-positive cells) (**Fig. 3b**). On a behavioral level, we found that locomotion and anxiety-related behavior, as measured in the open field and EPM tests, was unaltered in 138-sponge^{PV} mice compared to their littermate controls (**suppl. Fig. 3b, c**). Likewise, in the Y-maze test, no genotype-dependent differences in spontaneous alternations were observed (**Fig 3e**). However, similar as 138-sponge^{ub} mice (**Fig. 1c, d**), 138-sponge^{PV} mice showed impairments in behavioral tasks addressing short-term memory, such as the Y-maze novelty preference (**Fig. 3c**) and NOR (**Fig. 3d**) tests. These results demonstrate that miR-138-5p activity in PV-positive interneurons is required to sustain proper short-term memory. Next, we investigated

electrophysiological alterations that might underlie the observed short-term memory deficits. In hippocampal CA1 pyramidal neurons, which are the main targets of PV-positive interneurons in the hippocampal circuit, frequency of miniature inhibitory postsynaptic current (mIPSC) was significantly increased in 138-sponge^{PV} as compared to control slices, but neither amplitude, nor rise or decay time were changed (**Fig. 3f**, **suppl. Fig. 3d, e, f**). The total number of PV-positive interneurons in the hippocampus was similar between 138-sponge^{PV} and 138-floxed mice (**suppl. Fig. 3a**), suggesting that mIPSC frequency changes either result from an increased number of inhibitory presynaptic boutons synapsing onto pyramidal cells or an enhanced neurotransmitter release. To distinguish between these possibilities, we first analyzed presynaptic boutons contacting CA1 pyramidal cells by staining slices obtained from 138-floxed and 138-sponge^{PV} mice with antibodies against PV and the vesicular GABA transporter (VGAT). Our analysis revealed no significant difference in PV-positive presynaptic boutons impinging onto the somata of CA1 pyramidal cells between 138-sponge^{PV} mice and their littermate controls (**Fig.3g**). To probe for changes in presynaptic release probability, we first recorded extracellularly stimulated inhibitory paired-pulse ratios (iPPRs) in CA1 pyramidal cells but did not observe differences between the two groups (**suppl. Fig. 3g**). Finally, we performed paired whole-cell recordings between presynaptic putative fast-spiking PV-positive interneurons in stratum pyramidale (**suppl. Fig. 3h**) and postsynaptic CA1 pyramidal cells. The analysis of unitary connections revealed increased, albeit not significant, uIPSC amplitudes (including failures of transmission) and success rates (i.e. an action potential elicits an IPSC) in 138-sponge^{PV} mice as compared to their control littermates (**Fig. 3h**). However, we did not observe significant changes in paired-pulse ratio (**Fig. 3i**). Our further analysis though revealed a significant decrease of the coefficient of variance (CV), indicative of more reliable unitary synaptic connections between PV-positive interneurons and CA1 pyramidal neurons in 138-sponge^{PV} mice (**Fig. 3j**). These findings may also explain why mIPSC frequency was found to be altered as these inhibitory currents reflect inputs of many GABAergic neurons onto a single excitatory pyramidal neuron. In conclusion, CA1 pyramidal neurons in 138-sponge^{PV} mice receive increased inhibitory GABAergic synaptic transmission from putative fast-spiking PV-positive interneurons without detectable changes in perisomatic inhibitory bouton density.

Discussion

Here, we describe a central role for the brain-enriched miRNA miR-138-5p in the regulation of inhibitory GABAergic transmission in the hippocampus. Particularly, we find that cell type-specific inhibition of miR-138-5p in PV-positive interneurons enhances the reliability of unitary synaptic connections from putative fast-spiking PV-positive interneurons onto CA1 pyramidal neurons. The resulting increase in neurotransmitter release at this synapse is possibly due to an increase in the number of presynaptic release sites within individual boutons (Sakamoto et al., 2018), as we observed a decrease in CV, but did not detect significant changes in release probability. PV-positive interneurons are the main source of feedforward inhibition onto pyramidal neurons (Pouille and Scanziani, 2001) and have been functionally linked to working memory (Murray et al., 2011), possibly via controlling gamma oscillations (Hajos et al., 2004). We therefore propose a model whereby miR-138-5p activity in PV-positive interneurons is regulating neurotransmitter release, thereby keeping pyramidal cell output in a range required for proper information processing. Since miR-138-5p controls dendritic spine morphogenesis in cultured hippocampal pyramidal neurons (Siegel et al., 2009), it might further regulate E-I balance in the hippocampal circuitry by controlling pyramidal neuron excitatory input. The absence of changes in excitatory synaptic transmission in the hippocampus of 138-sponge^{ub} mice might be due to ineffective silencing of the highly abundant miR-138-5p in pyramidal neurons via our approach.

The molecular mechanisms downstream of miR-138-5p inactivation leading to enhanced inhibition remain to be elucidated, but likely involve upregulation of proteins organizing inhibitory presynaptic function, such as Erbb4 and Rims3. In line with this hypothesis, Erbb4 has been shown to control GABAergic transmission (Fazzari et al., 2010; Wang et al., 2018) and working memory (Tian et al., 2017; Wen et al., 2010), whereas Rims3 physically and functionally interacts with presynaptic voltage-dependent Ca^{2+} channels (VDCCs) and increases neurotransmitter release (Takada et al., 2015).

Mutations in Erbb4 and Rims3 have been associated with schizophrenia and ASD, respectively (Kumar et al., 2010; Nicodemus et al., 2006), while miR-138 expression correlates with short-term recognition memory in mice (Tatro et al., 2013) and memory

226 performance in humans (Schroder et al., 2014). Thus, miR-138 might be a promising
227 target for the treatment of cognitive deficits associated with ASD and schizophrenia.
228

Materials and methods

Construct design and cloning

MiR-138 sponge:

MiR-138 sponge was cloned into the BsrGI and HindIII restriction sites of a modified pAAV-6P-SEWB backbone, where the GFP has previously been replaced with dsRed(Christensen et al., 2010). Different number of binding sites were tested, and the plasmid containing 6 binding sites was chosen for further experiments which included the virus production for the creation of the mouse lines.

MiR-138 sponge imperfect binding site: 5' CGGCCTGATTCGTTCACCAGT 3'; spacer sequence: 5' TTTTT 3'; *Control sponge sequence*: 5' TGTGACTGGGGGCCAGAGG 3'; spacer sequence: 5' CAGTG 3'

pGL3-138 perfect binding site (pbds) vector:

The oligonucleotides were designed without any specific overhangs to allow blunt end cloning in both directions for a perfect binding site reporter and an antisense control reporter. They were annealed and ligated into a pGL3 promotor vector (Promega, Mannheim) expressing firefly luciferase. For cloning, the pGL3 vector was before digested with XbaI and the ends were blunted to insert the binding sites via blunt end cloning at the 3'end of the firefly open reading frame (ORF). After cloning, several clones were sequenced to determine sense- and antisense reporter.

138 pbds reporter FW:

5'CTAGACGGCCTGATTCACAACACCAGCTACCGGCCTGATTCACAACACCAGC TGGATCC 3'

138 pbds reporter REV:

5'CTAGCGGATCCAGCTGGTGTTGTGAATCAGGCCGGTAGCTGGTGTTGTGAAT CAGGCCGT 3'

AAV-miR-138 dual sensor construct

An EcoR1-BglII PCR fragment spanning the pCMV promoter, mCherry coding sequence and SV40 poly adenylation signal was amplified using C1-mCherry (Addgene, 632524) as template. The PCR product was cloned into the BGlII/EcoR1 sites of the AAV-hSyn-EGFP (Addgene, 114213), upstream of the human Synapsin 1

promoter. Two miR-138 perfectly complementary binding sites were cloned into the SpeI and HIndIII restriction sites, between the EGFP coding sequence and WPRE element of AAV-hSYN-GFP, to generate the final AAV-138 sensor:

138 perfect binding sites FW:

5'CTAGACGGCCTGATTCACAACACCAGCTACCGGCCTGATTCACAACACCAGC TGGATCC 3'

138 perfect binding site REV:

5'CTAGCGGATCCAGCTGGTGTTGTGAATCAGGCCGGTAGCTGGTGTTGTGAAT CAGGCCGT 3'

Luciferase constructs:

pmirGLO dual-luciferase expression vector reporter (Promega, Madison, WI, USA) was used to clone portions of 3' untranslated regions of the investigated mRNAs. XhoI and SalI restriction enzymes were used.

ErbB4 wild type sequence:

5'TTGAATGAAGCAATATGGAAGCAACCAGCAGATTAACTAATTTAAATACTTC 3';

ErbB4 138-mutant sequence:

5'TTGAATGAAGCAATATGGAAGCAgCatGaAGATTAACTAATTTAAATACTTC 3';

Rims3 wild type sequence:

5'GCCTCAGTCACCAGCTCTGTACCAGCAATACTCACCCCTCCACCTCCCTGACT T 3';

Rims3 138-mutant sequence:

5'GCCTCAGTgAtatcCTCTGTACCAGCAATACTCACCCCTCCACCTCCCTGACTT 3';

Primary neuronal cell culture

Cultures of dissociated primary cortical and hippocampal neurons from embryonic day 18 (E18) Sprague-Dawley rats (Janvier, France) were prepared and cultured as described previously(Schratt et al., 2006). Animal euthanasia was approved by the local cantonal authorities (ZH196/17).

Transfection

Transfection of primary neurons was performed using Lipofectamine 2000 (Invitrogen, Karlsruhe). For each well of a 24-well plate a total of 1 ug DNA was mixed with a 1:50

dilution of Lipofectamine in NB/NBP medium. After an incubation of 20 min at room temperature, it was further diluted 1:5 in NB/NBP medium and applied to the cells. Neurons were incubated for 2 h with the mix. A 1:1000 dilution of APV (20mM) in NB+/NBP+ was applied for 45-60 min afterwards before exchanging with NB+/NBP+.

Luciferase assay

Luciferase assays were performed using the dual-luciferase reporter assay system on a GloMax R96 Microplate Luminometer (Promega). pmirGLO dual-luciferase expression vector reporter (Promega, Madison, WI, USA) was used to clone portions of 3' untranslated regions of the investigated mRNAs. PcDNA3 was used to balance all amounts to a total of 1 ug DNA per condition.

Animal lines

The C57BL/6NTac-*Gt(ROSA)26So* $^{tm2459(LacZ,\ antimir\_138)\ Arte}$ (hereafter named "138-floxed") mouse lines was created at TaconicArtemis GmbH (Cologne, Germany). The targeting strategy allowed the generation of a constitutive LacZ-miRNA138 Sponge Knock-In (KI) allele in the C57Bl/6 mouse ROSA26 locus via targeted transgenesis. The presence of the loxP-flanked transcriptional STOP cassette is expected to terminate the transcription from the CAG promoter and thus prevent the expression of the NLS-LacZ miRNA138 Sponge cDNA, which allows this line to be used as a control (138-floxed line). The constitutive KI allele was obtained after Cre-mediated removal of the loxP-flanked transcriptional STOP cassette from the conditional KI allele, by crossing the 138-flox line with a B6.C-Tg(CMV-Cre)1Cgn (CMV-CRE) line, which allows the expression of the sponge construct (138-sponge^{ub} mice).). In all experiments, heterozygous male mice were used. The 138-sponge^{PV} line was generated by crossing 138-floxed line with a previously characterized B6;129P2-*Pvalb*$^{tm1(cre)Arbr}$/J (PV-CRE) line.

Behavioral Experiments

Animals were housed in groups of 3-5 per cage, with food and water *ad libitum*. All experiments were performed on adult male mice (3-5 months old). The animal house had an inverted light-dark cycle, all testing was done during the dark phase (8 am-8 pm). Mice were handled for 10 minutes for 5 days before the experiments began. All measures were analyzed by Noldus Ethovision xt 14, unless

stated differently. During the experimental phase, mice were transported individually and allowed to acclimatize to the experimental room in a holding cage for at least 20 minutes before the beginning of the task. At the end of each experiment they were transported back into the animal storage room in their holding cage and placed back into their original home cage with their littermates. 10ml/l detergent (For, Dr .Schnell AG) was used to clean equipment in between trials. Tasks which required the use of the same apparatus were scheduled at least 4 days apart. Two separate cohorts of mice were tested (7 mice each). No cohort-specific differences were found. The behavioral essays were performed from the least to the most stressful: home cage activity, open field, y maze, elevated plus maze, Novel object recognition, contextual fear conditioning. All animal experiments were performed in accordance with the animal protection law of Switzerland and were approved by the local cantonal authorities (ZH017/18).

Open field (OFT):

OFT was performed as described previously (Lackinger et al., 2019). Each session lasted 30 minutes.

Y maze:

Spontaneous alternation: mice were placed in a Y shaped maze (8.5cm width x 50cm length x 10cm height) for 5 minutes. They were free to explore the whole maze and the alternation between the arms was calculated.
Novelty preference test: mice were given 5 minutes to explore 2 arms of the maze during the familiarization phase. A door made from the same Plexiglas used for the walls was used to prevent the access of the subjects into the third arm. At the end of the familiarization phase, mice were placed in their holding cage for 90 seconds, while the apparatus was cleaned to avoid olfactory trails. Mice were then placed back into the maze for the test phase, where all three arms where accessible. Preference ratio between the familiar and new arm was then scored based on the time spent in those arms.

Elevated Plus Maze:

The maze was elevated 60 cm from the floor, with two arms enclosed by dark Plexiglas walls (5cm width × 30cm length × 15cm height), two opposing open arms and a central platform/intersection. Experiments were conducted in a homogenously illuminated room, with the maze placed in the center of the room. Mice were placed in the central platform of the elevated plus maze. The position and motion of the animals was

automatically determined and recorded for 5 min. Time spent and distance travelled in the different arms was scored.

Novel Object Recognition:

Objects were based on the Nature protocol published previously (Leger et al., 2013). They were tested beforehand to assess that no object was preferred, and they were randomized between trials and genotypes. Subjects were placed in the open field arena with two items of the same objects for a 5 minute familiarization period. After a 90 seconds break in their holding cage while the arena and the objects was cleaned and one object changed, the mice were put back in the arena for the test phase for 5 minutes. Time spent exploring the new object was scored manually. Scoring took into consideration the time spent exploring the two objects and the number of visits (nose of the experimental mouse within a 3cm radius from the object).

Contextual Fear Conditioning

This task was performed as previously described (Siegert et al., 2015). Briefly, mice were placed in the open field arena with Plexiglas walls and a metal grid bottom inside the multiconditioning chambers and a metal grid bottom (TSE fear conditioning system, TSE Systems, Germany). They were habituated for 3 min, then foot-shocked (2 s, 0.8 mA constant current) and returned to their home cages. After 24 h, mice were placed in the conditioning chamber. Freezing, defined as a total lack of movement except for heartbeat and respiration, was scored for a 3 minutes period.

RNAseq

RNA extraction Adult male mice (4 months old) were anaesthetized with isoflurane (Baxter, Unterschleißheim, Germany) and then quickly cervically dislocated and decapitated. Hippocampal tissue was dissected and freshly processed (RNA was extracted using mirVana microRNA Isolation Kit (Life Technologies) according to the manufacturer's instructions.

Stranded polyA+ enriched RNA sequencing libraries were prepared at the GENCORE (EMBL, Genomics Core Facility, Heidelberg, Germany) and sequenced on an Illumina HiSeq 2000 machine using a 50nt paired-end protocol (Lackinger et al., 2019).

Quantitative real-time PCR

qPCR was performed as described earlier (Valluy et al., 2015). Primer sequences are given below.

ErbB4 FW: 5'GACTCCAATAGGAATCAGTTTGTC 3'

ErbB4 REV: 5' TACTGGAGCCTCTGGTATGG 3'

Rims3 FW: 5' GCATCAGCGGTGAGATCTGT 3'

Rims3 REV: 5' CTGGGTCAAGCCGACGATAG 3'

Imaging:

Image acquisition was done with the experimenter being blinded to the different conditions. Pictures were taken on a confocal laser scanning microscope equipped with an Airyscan detector (LSM880, Zeiss). Image analysis was carried out on Fiji (ImageJ).

PV bouton count: a 63x oil objective was used to take images from CA1 hippocampal region immunostained with PV, VGAT and Hoechst was used to counterstain the nuclei (further details in the immunostaining section). The number of PV+ and VGAT+ en passant boutons around the nuclear perimeter were counted and normalized to the total length of the perimeter.

PV cell quantification: a 20x objective was used and PV+ cells were counted on a maximum projection intensity of the CA1 region immunostained with PV (Hoechst was used to counterstain nuclei; further details in the immunostaining section). The number of PV+ cells was normalized to a defined region of interest (230μm x 460μm).

Viral mir-138 sensor: tilescans were taken with a 20x objective of the infected hippocampal region. Intensity of GFP signal was normalized on the mCherry signal per cell.

Spine analysis

In vitro: Hippocampal neurons were transfected at DIV 10 with 200 ng of GFP and the indicated amount of either miR-138-6x-sponge, CTR sponge, AAV backbone or the Cholesterol-modified 2'O-Me-oligonucleotides ('antagomirs', Thermo Scientific, Karlsruhe. To balance all amounts to a total of 1 ug DNA per condition, PcDNA3 was used. At 18 DIV Cells were fixed using 4 % PFA for 15 min and mounted on glass slides using Aqua-Poly/Mount (Polysciences Inc., Eppelheim). The experimenter was blinded to all the conditions. The z-stack images of GFP-positive neurons exhibiting pyramidal morphology were taken with the 63x objective of a confocal laser scanning

microscope (Carl Zeiss, Jena). Eight consecutive optical sections of the dendrites were taken at a 0.4 μm interval with a 1024 x 1024 pixel resolution. Spine volumes were analyzed with the ImageJ software using the maximum intensity projections of the z-stack images. The GFP intensity of 150-200 spines per cell was measured and normalized to the total intensity of the dendritic tree. For each experimental condition, at least 18 representative neurons derived from three independent experiments were analyzed.

In vivo: brains from 3 months old 138-floxed and 138-sponge^{ub} mice were processed with FD Rapid GolgiStain Kit (Gentaur GmbH, PK401) according to the manufacturer's protocol. Pictures were taken with a Zeiss axio-observer 7 inverted wide field fluorescence microscope equipped with a Axiocam 702 mono Zeiss camera with an 100x oil objective. Dendritic spines were manually analyzed with Fiji (ImageJ).

Electrophysiology.

Hippocampal slices (300 µm thick) were prepared at 4 °C, as previously described (Winterer et al., 2019), from 138-floxed, 138-sponge^{ub} and 138-sponge^{PV} mice (age: 6-8 weeks) and incubated at 34°C in sucrose-containing artificial cerebrospinal fluid (sucrose-ACSF, in mM: 85 NaCl, 75 sucrose, 2.5 KCl, 25 glucose, 1.25 NaH2PO4, 4 MgCl2, 0.5 CaCl2, and 24 NaHCO3) for 0.5 h, and then held at room temperature until recording.

Whole cell patch clamp recordings were performed at 32 °C on an upright microscope (Olympus BX51WI) under visual control using infrared differential interference contrast optics. Data were collected with an Axon MultiClamp 700B amplifier and an Digidata 1550B digitizer and analyzed with pClamp 11 software (all from Molecular Devices). Signals were filtered at 2 kHz for miniature EPSCs and miniature IPSCs and digitized at 5 kHz. Stimulus evoked and unitary postsynaptic currents were filtered at 4 kHz, fast-spiking interneurons at 10 kHz, both were digitized at 100 kHz. Recording pipettes were pulled from borosilicate capillary glass (Harvard Apparatus; GC150F-10) with a DMZ-Universal-Electrode-Puller (Zeitz) and had resistances between 2 and 3 MΩ.

The extracellular solution (ACSF) was composed of (in mM) 126 NaCl, 2.5 KCl, 26 $NaHCO_3$, 1.25 NaH_2PO_4, 2 $CaCl_2$, 2 $MgCl_2$ and 10 glucose. For excitatory postsynaptic currents (EPSCs) measured in CA1 pyramidal cells and for fast-spiking interneurons the intracellular solution was composed of 125 K-Gluconate, 20 KCl 0.5 EGTA, 10

HEPES, 4 Mg-ATP, 0.3 GTP and 10 Na_2-phosphocreatine (adjusted to pH 7.3 with KOH). Cells were held at -70mV for miniature EPSC (mEPSCs) and at -60mV for stimulus evoked excitatory postsynaptic currents (eEPSCs). 1µM Gabazine was added to isolate AMPA-mediated postsynaptic currents, additionally 1µM TTX for mEPSCs. For inhibitory postsynaptic currents (IPSCs) intracellular solution was composed of 135 Cs-Gluconate, 5 KCl, 2 NaCl, 0.2 EGTA, 10 HEPES, 4 Mg-ATP, 0.3 GTP and 10 Na_2-phosphocreatine (adjusted to pH 7.3 with CsOH). Cells were held at +10mV for miniature IPSC (mIPSCs) and at -10mV for stimulus evoked and unitary inhibitory postsynaptic currents (eIPSCs and uIPSCs). 25µM AP-5, 10µM NBQX and 10µM SCH 50911 were added to isolate GABAa-mediated postsynaptic currents for eIPSCs, additionally 1µM TTX for mIPSCs. Synaptic currents were evoked by mono-polar stimulation with a patch pipette filled with ACSF and positioned in the middle of CA1 stratum radiatum for eEPSCs and in stratum pyramidale for eIPSCs. Series resistance of CA1 pyramidal neurons (not compensated; range, from 7.0 to 19.7 MΩ; median, 11.2 MΩ; IQR, 2.5 MΩ) was monitored and recordings were discarded if series resistance changed by more than 20%. Membrane potentials were not corrected for liquid junction potential.

For paired recordings, whole cell configuration was first established in putative fast-spiking interneurons. Cells were selected based on morphological appearance in stratum pyramidale of hippocampal CA1, on fast-spiking properties and on input resistance characteristic for PV-positive interneurons (Que et al., 2021)(**suppl. Fig. 3h**). Subsequently whole cell recordings were made from postsynaptic CA1 pyramidal neurons residing in close proximity to the presynaptic fast-spiking interneuron. Presynaptic fast-spiking interneurons were held in current-clamp mode and series resistance was compensated with the automatic bridge balance of the amplifier. The mean resting potential of the presynaptic fast-spiking interneurons was -65 ± 4.1mV (mean ± sd; **suppl. Fig. 3h)**. Fast-spiking interneurons were stimulated at 1Hz for uIPSCs and at 0.03Hz for paired pulse uIPSCs. To characterize the discharge behavior of fast-spiking interneurons, depolarizing steps (50pA) of 1500ms were applied. The spiking frequency (**suppl. Fig. 3h**) was determined at 800 to 1000pA current injection. Input resistance was calculated from the mean deviation from baseline of steady state voltage responses evoked by -150, -100 and -50 pA current injections.

499
500
501
502 **Cell type enrichment analysis**
503 For the cell type enrichment analysis, we used the single-cell data and annotation from
504 Zeisel et al. (2018). We downloaded single-cell count data and annotation from
505 https://storage.googleapis.com/linnarsson-lab-loom/l5_all.loom, restricted it to
506 hippocampus cells, and aggregated to the pseudo-bulk level using muscat (Crowell et
507 al., 2020) and the authors' cell identities. We retained only cell types represented by
508 more than 50 cells, and normalized using TMM (Robinson and Oshlack, 2010). For
509 each gene, we then identified the cell type in which it was the most highly expressed,
510 forming gene sets for each cell type. We then created a sponge differential expression
511 signature by multiplying the sign of the foldchange with the -log10(p-value) of each
512 gene, and looked for enrichment of gene sets in this signature using fgsea
513 (Korotkevich et al., Biorxiv 2021, doi: 10.1101/060012).
514
515
516 **GO enrichment analysis**
517 The R Bioconductor package TopGo (v.2.42.0) was used to perform Gene Ontology
518 enrichment analysis, essentially as in (Lackinger et al., 2019).
519 To sum up, genes were annotated with the “Cellular Component” ontology and
520 significantly changed genes subsequently tested against the expressed background.
521 For the main figure we plotted the Top10 GO-Terms ranked by significance (filtering
522 out those with more than 200 annotated genes).
523
524 **miRNA binding site analysis**
525 Mouse 3’UTR positions of predicted conserved microRNA binding sites were
526 downloaded from Targetscan (version 7.2)(Agarwal et al., 2015) and filtered for the
527 seed of miR-138-5p. Putative miR-138 targets (including site-type information) were
528 then aligned with the genes and log fold changes (logFC) as obtained by the
529 differential expression analysis. Plotted is the cumulative proportion (logFC rank (-1) /
530 number of genes (-1)) over the logFC.
531
532 **Single-molecule fluorescence *in situ* hybridization (smFISH)**

smFISH for miRNA detection on hippocampal neuron cultures was performed using the QuantiGene ViewRNA miRNA Cell Assay kit (Thermo Fisher) according to the manufacturer's protocol with slight modifications. To preserve dendrite morphology, protease treatment was reduced to a dilution of 1:10,000 in PBS for 45 sec. smFISH for mRNA detection was performed using the QuantiGene ViewRNA ISH Cell Assay kit (Thermo Fisher) as previously described (Valluy et al., 2015), but omitting the protease treatment. After completion of the FISH protocol, cells were washed with PBS, pre-blocked in gelatin detergent buffer and processed for immunostaining. Pictures represent maximum intensity projections of z-stack images taken on a confocal laser scanning microscope equipped with an Airyscan detector (LSM880, Zeiss).

Stereotactic surgery

The viral vector (aaAAV-9/2 [hCMV-mCherry-SV40p(A)]rev-hSyn1-EGFP-2x (miR-138-5p)-WPRE-SV40p(A)) was produced by the local Viral Vector Facility (VVF9 of the Neuroscience Center Zurich). The produced virus had a physical titer of 6.1 x10e^{12} vector genomes/ml. Stereotactic brain injections were performed on two- to three-month-old 138-floxed and 138-sponge^{ub} mice as previously described(Zerbi et al., 2019)). Briefly, mice were anesthetized with isoflurane and subsequentially placed onto the stereotaxic frame. Before and after the procedure, animals received subcutaneous injection of 2 mg/kg Meloxicam for analgesia and local anaesthetic (Emla cream 5% lidocaine, 5% prilocaine) was distributed on the head. Animals were injected bilaterally with 1µl of virus into the dorsal hippocampus (coordinates from bregma: anterior/posterior −2.1 mm, medial/lateral ± 1.5 mm, dorsal/ventral −1.8 mm) and 1µl of virus in the ventral hippocampus (coordinates from bregma: anterior/posterior −3.3 mm, medial/lateral ± 2.75 mm, dorsal/ventral −4.0 mm). Post-operative health checks were carried on over the three days after surgery.

Tissue collection

Animals were sacrificed by intraperitoneal injection of pentobarbital (150 mg/kg). When in deep anaesthesia, mice were perfused intracardially with ice-cold PBS pH 7.4, followed by perfusion with 4% paraformaldehyde in PBS pH 7.4. The brains were then isolated and postfixed for 2-3h (138-floxed; 138-sponge^{PV} mice) or overnight

(138-flox and 138-sponge^{ub} mice) at 4°C. The fixed tissue was placed in sucrose solution (30% sucrose in PBS) for 24h and frozen in tissue mounting medium (OCT mounting media, VWR chemicals). The tissue was coronally sectioned at 50-60µm thickness on a cryostat, immediately placed in ice-cold PBS and subsequentially conserved in cryoprotectant solution (15% glucose, 30% ethylene glycol, 5mM $NaH_2PO_4*H_2O$, 20mM $Na_2HPO_4*2H_2O$) at -20°C.

Immunohistochemistry

For immunofluorescence, cryosections were washed in ice-cold PBS for 30 minutes, placed on microscope slides (Menzel-Gläser SUPERFROST PLUS, Thermo Scientific) and air-dried for 5-10 min. Afterwards, permeabilization was performed by incubating sections in permeabilization solution (0.5% Triton X-100 in PBS) for 30 min at room temperature, followed by a blocking step in blocking buffer (0.5% Triton X-100, 300mM NaCl, 10% Normal Goat Serum in PBS) with addition of blocking Reagent (VC-MKB-2213, Adipogen Life Sciences, 1:10 dilution) for 1h at room temperature. Cryosections were washed in PBS twice for 10 min at room temperature and incubated with primary antibodies in blocking buffer overnight at 4°C. Subsequentially, the sections were washed 3 times with blocking buffer, incubated with secondary antibodies and Hoechst 33342 in blocking buffer for 1h at room temperature, washed again three times in blocking buffer, washed in PBS, air-dried and mounted with Aqua-Poly/Mount (POL18606, Polysciences).

Statistics

Statistical analysis was performed on either GraphPad Prism 8.0 or RStudio. Plots were generated in R, mainly using the packages ggplot2, ggsci, ggrepel and scales. For data sets with n>4, Box plots (Tukey style) were used. For data sets with n<5, average +/- s.d., including individual data points, is shown.
The detailed parameters (n, p-value, test) for the statistical assessment of the data are provided in the figure legends.

Further reagents:

<u>smFISH probes:</u>

miR-138 (FastRed); VM1-10093-VCP. Erbb4 (488); VC4-3146482-VC. Rims3 (488); VC4-3146880-VCP. Camk2a (488); VC4-15081-VC. Camk2a (647); VC6-11639-VCP. Gad2 (647); VC6-16451-VCP.

Antibodies:

Rabbit αGAD65+67 (Abcam, ab11070, 1:100). Mouse αMAP2 (Sigma-Aldrich, M9942, 1:1,000). Rabbit αGFAP (Dako, Z0334, 1:1,000). Mouse αParvalbumin (SWANT, 235, 1:1,000). Rabbit αVGAT (Synaptic Systems, 131 003, 1:1,000). Rabbit αmCherry (Abcam, ab167453, 1:1,000). Chicken αbeta Galactosidase (Abcam, ab9361, 1:4,000). Donkey αMouse Alexa Fluor 488 (Invitrogen, A21202, 1:500). Goat αRabbit Alexa Fluor 546 (Invitrogen, A11010, 1:500). Goat αChicken Alexa Fluor 546 (Invitrogen, A11040, 1:500). Donkey αMouse Alexa Fluor 647 (Invitrogen, A31571, 1:500). Hoechst 33342 (Thermo Fisher, 62249).

Acknowledgments

We are grateful to S. Brown and M. Müller for valuable comments on the manuscript, T. Wüst and C. Furler for excellent technical assistance, T. Germade for help with bioinformatics, D. Colameo for help with animal perfusions and A. Loye for help with histology. This work was supported by grants from the DFG (SCHR 1136/4-2) and the ETH (24 18-2 (NeuroSno).

Author contributions:

RD performed behavioral tasks, qPCR, luciferase assays, histology, plasmid cloning and wrote the manuscript. KW performed in vitro sponge validation, histology and RNA preparation for RNA-seq. CG performed histology and stereotactic injections. SB designed the sponge construct and performed FISH. RF performed plasmid cloning. MS, CD and PLG performed bioinformatics analysis. JW performed electrophysiological recordings, wrote the manuscript and co-supervised the project. GS wrote the manuscript and supervised the project.

Data and code availability

RNA-seq data has been deposited to GEO (accession no. GSE173982).

The following figures have associated raw data: Fig. 2, suppl. Fig. 2.

Competing interests:

The authors declare no competing interests.

References:

Agarwal, V., Bell, G.W., Nam, J.W., and Bartel, D.P. (2015). Predicting effective microRNA target sites in mammalian mRNAs. Elife *4*.

Bartel, D.P. (2018). Metazoan MicroRNAs. Cell *173*, 20-51.

Booker, S.A., and Vida, I. (2018). Morphological diversity and connectivity of hippocampal interneurons. Cell Tissue Res *373*, 619-641.

Christensen, M., Larsen, L.A., Kauppinen, S., and Schratt, G. (2010). Recombinant Adeno-Associated Virus-Mediated microRNA Delivery into the Postnatal Mouse Brain Reveals a Role for miR-134 in Dendritogenesis in Vivo. Frontiers in neural circuits *3*, 16.

Crowell, H.L., Soneson, C., Germain, P.L., Calini, D., Collin, L., Raposo, C., Malhotra, D., and Robinson, M.D. (2020). muscat detects subpopulation-specific state transitions from multi-sample multi-condition single-cell transcriptomics data. Nat Commun *11*, 6077.

Del Pino, I., Rico, B., and Marin, O. (2018). Neural circuit dysfunction in mouse models of neurodevelopmental disorders. Curr Opin Neurobiol *48*, 174-182.

Ebert, M.S., and Sharp, P.A. (2010). MicroRNA sponges: progress and possibilities. Rna *16*, 2043-2050.

Fazzari, P., Paternain, A.V., Valiente, M., Pla, R., Lujan, R., Lloyd, K., Lerma, J., Marin, O., and Rico, B. (2010). Control of cortical GABA circuitry development by Nrg1 and ErbB4 signalling. Nature *464*, 1376-1380.

Hajos, N., Palhalmi, J., Mann, E.O., Nemeth, B., Paulsen, O., and Freund, T.F. (2004). Spike timing of distinct types of GABAergic interneuron during hippocampal gamma oscillations in vitro. J Neurosci *24*, 9127-9137.

He, M., Liu, Y., Wang, X., Zhang, M.Q., Hannon, G.J., and Huang, Z.J. (2012). Cell-type-based analysis of microRNA profiles in the mouse brain. Neuron *73*, 35-48.

Kumar, R.A., Sudi, J., Babatz, T.D., Brune, C.W., Oswald, D., Yen, M., Nowak, N.J., Cook, E.H., Christian, S.L., and Dobyns, W.B. (2010). A de novo 1p34.2 microdeletion identifies the synaptic vesicle gene RIMS3 as a novel candidate for autism. J Med Genet *47*, 81-90.

Lackinger, M., Sungur, A.O., Daswani, R., Soutschek, M., Bicker, S., Stemmler, L., Wust, T., Fiore, R., Dieterich, C., Schwarting, R.K.*, et al.* (2019). A placental mammal-specific microRNA cluster acts as a natural brake for sociability in mice. EMBO Rep *20*.

Leger, M., Quiedeville, A., Bouet, V., Haelewyn, B., Boulouard, M., Schumann-Bard, P., and Freret, T. (2013). Object recognition test in mice. Nat Protoc *8*, 2531-2537.

Markram, H., Toledo-Rodriguez, M., Wang, Y., Gupta, A., Silberberg, G., and Wu, C. (2004). Interneurons of the neocortical inhibitory system. Nat Rev Neurosci *5*, 793-807.

McNeill, E., and Van Vactor, D. (2012). MicroRNAs shape the neuronal landscape. Neuron *75*, 363-379.

Murray, A.J., Sauer, J.F., Riedel, G., McClure, C., Ansel, L., Cheyne, L., Bartos, M., Wisden, W., and Wulff, P. (2011). Parvalbumin-positive CA1 interneurons are required for spatial working but not for reference memory. Nat Neurosci *14*, 297-299.

Nicodemus, K.K., Luna, A., Vakkalanka, R., Goldberg, T., Egan, M., Straub, R.E., and Weinberger, D.R. (2006). Further evidence for association between ErbB4 and schizophrenia and influence on cognitive intermediate phenotypes in healthy controls. Mol Psychiatry *11*, 1062-1065.

Pelkey, K.A., Chittajallu, R., Craig, M.T., Tricoire, L., Wester, J.C., and McBain, C.J. (2017). Hippocampal GABAergic Inhibitory Interneurons. Physiological reviews *97*, 1619-1747.

Pouille, F., and Scanziani, M. (2001). Enforcement of temporal fidelity in pyramidal cells by somatic feed-forward inhibition. Science *293*, 1159-1163.

689 Qiu, F., Mao, X., Liu, P., Wu, J., Zhang, Y., Sun, D., Zhu, Y., Gong, L., Shao, M., Fan, K., *et al.*
690 (2020). microRNA Deficiency in VIP+ Interneurons Leads to Cortical Circuit Dysfunction. Cereb
691 Cortex *30*, 2229-2249.
692 Que, L., Lukacsovich, D., Luo, W., and Foldy, C. (2021). Transcriptional and morphological
693 profiling of parvalbumin interneuron subpopulations in the mouse hippocampus. Nat
694 Commun *12*, 108.
695 Rico, B., and Marin, O. (2011). Neuregulin signaling, cortical circuitry development and
696 schizophrenia. Curr Opin Genet Dev *21*, 262-270.
697 Robinson, M.D., and Oshlack, A. (2010). A scaling normalization method for differential
698 expression analysis of RNA-seq data. Genome Biol *11*, R25.
699 Rubenstein, J.L., and Merzenich, M.M. (2003). Model of autism: increased ratio of
700 excitation/inhibition in key neural systems. Genes Brain Behav *2*, 255-267.
701 Sakamoto, H., Ariyoshi, T., Kimpara, N., Sugao, K., Taiko, I., Takikawa, K., Asanuma, D., Namiki,
702 S., and Hirose, K. (2018). Synaptic weight set by Munc13-1 supramolecular assemblies. Nat
703 Neurosci *21*, 41-49.
704 Schratt, G. (2009). microRNAs at the synapse. Nat Rev Neurosci *10*, 842-849.
705 Schratt, G.M., Tuebing, F., Nigh, E.A., Kane, C.G., Sabatini, M.E., Kiebler, M., and Greenberg,
706 M.E. (2006). A brain-specific microRNA regulates dendritic spine development. Nature *439*,
707 283-289.
708 Schroder, J., Ansaloni, S., Schilling, M., Liu, T., Radke, J., Jaedicke, M., Schjeide, B.M.,
709 Mashychev, A., Tegeler, C., Radbruch, H., *et al.* (2014). MicroRNA-138 is a potential regulator
710 of memory performance in humans. Front Hum Neurosci *8*, 501.
711 Siegel, G., Obernosterer, G., Fiore, R., Oehmen, M., Bicker, S., Christensen, M.,
712 Khudayberdiev, S., Leuschner, P.F., Busch, C.J., Kane, C., *et al.* (2009). A functional screen
713 implicates microRNA-138-dependent regulation of the depalmitoylation enzyme APT1 in
714 dendritic spine morphogenesis. Nat Cell Biol *11*, 705-716.
715 Siegert, S., Seo, J., Kwon, E.J., Rudenko, A., Cho, S., Wang, W., Flood, Z., Martorell, A.J.,
716 Ericsson, M., Mungenast, A.E., *et al.* (2015). The schizophrenia risk gene product miR-137
717 alters presynaptic plasticity. Nat Neurosci *18*, 1008-1016.
718 Sohal, V.S., and Rubenstein, J.L.R. (2019). Excitation-inhibition balance as a framework for
719 investigating mechanisms in neuropsychiatric disorders. Mol Psychiatry *24*, 1248-1257.
720 Takada, Y., Hirano, M., Kiyonaka, S., Ueda, Y., Yamaguchi, K., Nakahara, K., Mori, M.X., and
721 Mori, Y. (2015). Rab3 interacting molecule 3 mutations associated with autism alter regulation
722 of voltage-dependent Ca(2)(+) channels. Cell Calcium *58*, 296-306.
723 Tatro, E.T., Risbrough, V., Soontornniyomkij, B., Young, J., Shumaker-Armstrong, S., Jeste,
724 D.V., and Achim, C.L. (2013). Short-term recognition memory correlates with regional CNS
725 expression of microRNA-138 in mice. Am J Geriatr Psychiatry *21*, 461-473.
726 Tian, J., Geng, F., Gao, F., Chen, Y.H., Liu, J.H., Wu, J.L., Lan, Y.J., Zeng, Y.N., Li, X.W., Yang, J.M.,
727 *et al.* (2017). Down-Regulation of Neuregulin1/ErbB4 Signaling in the Hippocampus Is Critical
728 for Learning and Memory. Molecular neurobiology *54*, 3976-3987.
729 Tuncdemir, S.N., Fishell, G., and Batista-Brito, R. (2015). miRNAs are Essential for the Survival
730 and Maturation of Cortical Interneurons. Cereb Cortex *25*, 1842-1857.
731 Valluy, J., Bicker, S., Aksoy-Aksel, A., Lackinger, M., Sumer, S., Fiore, R., Wust, T., Seffer, D.,
732 Metge, F., Dieterich, C., *et al.* (2015). A coding-independent function of an alternative Ube3a
733 transcript during neuronal development. Nat Neurosci *18*, 666-673.

734 Wang, H., Liu, F., Chen, W., Sun, X., Cui, W., Dong, Z., Zhao, K., Zhang, H., Li, H., Xing, G.*, et al.*
735 (2018). Genetic recovery of ErbB4 in adulthood partially restores brain functions in null mice.
736 Proc Natl Acad Sci U S A *115*, 13105-13110.
737 Wen, L., Lu, Y.S., Zhu, X.H., Li, X.M., Woo, R.S., Chen, Y.J., Yin, D.M., Lai, C., Terry, A.V., Jr.,
738 Vazdarjanova, A.*, et al.* (2010). Neuregulin 1 regulates pyramidal neuron activity via ErbB4 in
739 parvalbumin-positive interneurons. Proc Natl Acad Sci U S A *107*, 1211-1216.
740 Winterer, J., Lukacsovich, D., Que, L., Sartori, A.M., Luo, W., and Foldy, C. (2019). Single-cell
741 RNA-Seq characterization of anatomically identified OLM interneurons in different transgenic
742 mouse lines. Eur J Neurosci *50*, 3750-3771.
743 Zeisel, A., Hochgerner, H., Lonnerberg, P., Johnsson, A., Memic, F., van der Zwan, J., Haring,
744 M., Braun, E., Borm, L.E., La Manno, G.*, et al.* (2018). Molecular Architecture of the Mouse
745 Nervous System. Cell *174*, 999-1014 e1022.
746 Zerbi, V., Floriou-Servou, A., Markicevic, M., Vermeiren, Y., Sturman, O., Privitera, M., von
747 Ziegler, L., Ferrari, K.D., Weber, B., De Deyn, P.P.*, et al.* (2019). Rapid Reconfiguration of the
748 Functional Connectome after Chemogenetic Locus Coeruleus Activation. Neuron *103*, 702-
749 718 e705.
750
751

752

Figure legends

Figure 1

(a) Schematic overview of the strategy for generating 138-sponge^{ub} mice. **(b)** Cumulative probability plot of GFP/mCherry ratios from hippocampal neurons infected with a 138-pbds sensor construct; 138-floxed: n=105 cells from two mice, 138-sponge^{ub}: n=127cells from three mice; p= 0.02 (KS-test). Representative images are shown on the right. **(c)** Upper: schematic representation of the Y maze novelty preference task; lower: preference ratio calculated as time spent in novel arm vs. time spent in novel and familiar arm; 138-floxed n=12; 138-sponge^{ub} n=14; *p=0.013 (Student's two-tailed heteroscedastic t test). **(d)** Upper: schematic representation of the novel object recognition task; lower: exploration time presented as percentage of total time spent with either novel or familiar object; 138-floxed n=12; 138-sponge^{ub} n=12; **** p<0.00002; n.s. p=0.11 (Student's two tailed heteroscedastic t test). **(e)** Upper: schematic representation of the contextual fear conditioning task; lower: time (s) mice spent freezing 24 h after the foot shock was administrated; 138-floxed n=7; 138-sponge^{ub} n=7; n.s. p=0.97 (Student's two-tailed heteroscedastic t test). **(f)** mEPSC recording in CA1 pyramidal neurons. Upper panel: example traces; scale bar: 20 pA, 500 ms. Lower panel left: mEPSC amplitude (138-floxed: range, from 14.3 to 25.6 pA; median, 17.2 pA; interquartile range [IQR], 3.9 pA. 138-sponge^{ub}: range, from 14.1 to 25.2 pA; median, 17.4 pA; IQR, 3.1 pA; n.s. p=0.74 Student's two-tailed heteroscedastic t test). Lower panel right: mEPSC frequency (138-floxed: range, from 0.2 to 0.9 Hz; median, 0.5 Hz; IQR, 0.2 Hz. 138-sponge^{ub}: range, from 0.3 to 0.7 Hz; median, 0.5 Hz; IQR, 0.1 Hz; n.s. p=0.91 Student's two-tailed heteroscedastic t test). 138-floxed n=13 cells/4mice; 138-sponge^{ub} n=13cells/3mice. **(g)** Upper: representative images of Golgi-stained CA1 pyramidal neuron dendritic segments of the indicated genotypes. Lower: quantification of dendritic spine width (left) and density (number/μm; right) based on Golgi staining; 138-floxed: n=1312 spines from 15 cells and 3 mice; 138-sponge^{ub} n=1687 spines from 18 cells and 3 mice (n.s., p=0.25 (width); p=0.49 (density); Student's two tailed heteroscedastic t test)

Figure 2

(a) Volcano plot of differentially expressed genes (DEGs) obtained from polyA-RNAseq of total hippocampal RNA from 138-flox and 138-sponge^{ub} mice. N=3. Genes with FDR<0.05 are labeled blue (downregulated) or green (upregulated). Rims3 and Erbb4 are indicated. **(b)** Cumulative distribution plots of log_2-fold expression changes (138-sponge^{ub}/138-floxed) for genes either containing (targets, red curve) or not containing (non-targets, black curve) predicted miR-138 binding sites. p=2.55e^{-05} (KS-test). **(c)** Gene ontology (GO) term analysis for DEGs. Top ten enriched cellular component (CC) GO terms with less than 200 total genes are shown. **(d)** Enrichment analysis of DEGs in different brain cell types based on published single-cell RNA-seq data(Zeisel et al., 2018). Normalized enrichment score>0: upregulated in 138-sponge^{ub} mice. **(e)** Single-molecule FISH analysis of miR-138 (red) together with Camk2a or Erbb4 mRNA to label excitatory or inhibitory neurons, respectively. Hoechst was used to counterstain nuclei. GAD65/67 antibody staining was used to identify GABAergic neurons. Scale bar=100μm (upper); 20μm (lower left and center), 5μm (lower right). **(f)** qPCR analysis of ErbB4 and Rims3 mRNAs in total hippocampal RNA obtained from 138-floxed or 138-sponge^{ub} mice. U6 snRNA was used for normalization. n=3; *p=0.003, #p=0.04 (Student's two-tailed heteroscedastic t test); **(g-h)** Relative luciferase activity in rat cortical neurons (DIV9-12) transfected with Erbb4 (g) or Rims3 (h) 3'UTR constructs with (138mut) or without (wt) a mutation in the miR-138 binding site, together with miR-138 or negative control mimics. n=3 (Rims3), n=4 (Erbb4). Negative control mimic = 1. (g) *p=0.025, n.s. p= 0.09 (h) *p=0.002, n.s. p=0.23 (student's two-tailed heteroscedastic t test).

Figure 3

(a) Schematic overview of the strategy for generating miR-138 sponge^{PV} mice. **(b)** Beta-gal expression is restricted to PV expressing interneurons: 138-sponge^{PV} mice n=3mice. **(c)** Behavioral characterization of 138-sponge^{PV} mouse line**,** upper: schematic representation of the Y maze novelty preference task; lower: preference ratio calculated as time spent in novel arm vs. time spent in novel and familiar arm; 138-floxed n=10; 138-sponge^{PV} n=10; *p=0.021 (Student's two-tailed heteroscedastic

t test). **(d)** Upper: schematic representation of the novel object recognition task; Lower: exploration time presented as percentage of total time spent with either novel or familiar object; 138-floxed n=10; miR-138 sponge n=10;*p=0.035, n.s. p=0.57 (Student's two-tailed heteroscedastic t test). **(e)** Percentage of spontaneous alternations in the Y-Maze. 138-floxed n=10; 138-sponge^{PV} n=10; n.s. p=0.90 (student's two-tailed heteroscedastic t-test) **(f)** mIPSC frequency in CA1 pyramidal neurons. Upper panel: example traces, 138-floxed in orange, 138-songe^{PV} in red, scale bar: 50 pA, 200 ms. Lower panel: mIPSC frequency (138-floxed: range, from 1.6 to 10.2 Hz; median, 4.1 Hz; IQR, 1.5 Hz. 138-sponge^{PV}: range, from 3.6 to 15.2 Hz; median, 6.2 Hz; IQR, 4.2 Hz; ***p = 0.0007, Student's two-tailed heteroscedastic t test). 138-floxed n=22 cells/5mice; 138-sponge^{PV} n=23cells/5mice. **(g)** PV+, VGAT+ bouton density (number of boutons per CA1 pyramidal neuron cell perimeter based on Hoechst counterstain); 138-floxed: n=73 cells/3 mice; 138-sponge^{PV}: n=95 cells/5 mice; data represents the average per mouse ± s.d; n.s., p=0.65 (Student's two-tailed heteroscedastic t test); right panel: representative pictures (arrows point the PV+; VGAT+ boutons). **(h)** Unitary connections between presynaptic fast-spiking interneurons and postsynaptic CA1 pyramidal cells. Upper panel: example traces, 138-floxed: average of 50 sweeps in orange, 26 single sweeps in grey, 138-songe^{PV}: average of 50 sweeps in red, 26 single sweeps in grey; scale bar: 100 pA, 100 mV, 25 ms. Lower panel left: uIPSC amplitude (138-floxed: range, from 20.1 to 73.2 pA; median, 46.6 pA; IQR, 40.2 pA. 138-sponge^{PV}: range, from 19.3 to 123.8 pA; median, 64.5 pA; IQR, 64.4 pA; n.s. p=0.11 Student's two-tailed heteroscedastic t test). Lower panel right: Success rate (138-floxed: range, from 40 to 98 %; median, 86 %; IQR, 54 %. 138-sponge^{PV}: range, from 38 to 100 %; median, 98 %; IQR, 12 %; n.s. p=0.28 Student's two-tailed heteroscedastic t test). 138-floxed n=7 pairs/3mice; 138-sponge^{PV} n=9 pairs/5mice. **(i)** Paired pulse ratio of unitary connections. Upper panel: example traces, 138-floxed in orange, 138-songe^{PV} in red, uIPSCs are normalized to the first uIPSC, scale bar: 100 mV, 50 ms. Lower panel: PPR ($2^{nd}/1^{st}$ uIPSC) (138-floxed: range, from 0.42 to 0.85; median, 0.56; IQR, 0.10. 138-sponge^{PV}: range, from 0.44 to 0.62; median, 0.49; IQR, 0.14; n.s. p=0.34 Student's two-tailed heteroscedastic t test). 138-floxed n=7 pairs/3mice; 138-sponge^{PV} n=9 pairs/5mice. **(j)** Coefficient of variance (138-floxed: range, from 0.38 to 0.71; median, 0.44; IQR, 0.07. 138-sponge^{PV}: range, from 0.23 to 0.47; median, 0.38; IQR, 0.15; *p= 0.033, Student's two-tailed heteroscedastic t test). 138-floxed n=7 pairs/3mice; 138-sponge^{PV} n=9 pairs/5mice.

Supplementary Figure 1

(a) Relative luciferase activity in hippocampal neurons (DIV 12-17) transfected with pGL3 CTR (control) or pGL3-138 pbds (sensor) constructs. pGL3-CTR=1. n=3. **p=0.0044 (Student's two-tailed heteroscedastic t test). **(b)** Relative luciferase activity in hippocampal neurons (DIV 12-17) transfected as in a), in addition with either control (100ng) or increasing amounts of 138 sponge (25-100ng). pGL3-CTR/pGL3-138 only = 1. n=3, **p=0.005, *p=0.032, #p=0.045 (student's two-tailed heteroscedastic t test). **(c)** Quantification of relative dendritic spine volume in rat hippocampal neurons (DIV10-18) transfected with GFP and increasing amounts (25-100ng) of either control or 138 sponge. GFP only = 1. n = 3; each value represents at least 150 spines per cell, from 6 individual neurons per experiment. **p=0.006, *p=0.027, #p=0.004 (student's two-tailed heteroscedastic t-test). **(d)** Representative enzymatic b-Gal staining of cerebellar slices obtained from either 138-floxed (upper) or 138-sponge^{ub} (lower) mice. **(e)** Activity counts of mice from indicated genotypes monitored over 24 h in their home cage; 138-floxed: n=7, 138-sponge$^{ub:}$ n=7; data shown as mean ± s.d. **(f)** Percentage of spontaneous alternations in the Y-Maze. 138-floxed n=14; 138-sponge^{ub} n=14; n.s. p=0.43 (student's two-tailed heteroscedastic t-test). **(g)** Percentage of total distance travelled/time spent in the periphery or center of an open field arena during 30 min exploration by mice of the indicated genotypes; 138-floxed n=14; 138-sponge^{ub} n=14; n.s. p=0.14 (Two-way ANOVA). **(h)** Percentage of total time spent in the closed or open arms of an elevated plus maze (EPM) during 5 min exploration by mice of the indicated genotypes; 138-floxed: n=14; 138-sponge^{ub} :n=14; n.s. p=0.55 (Two-way ANOVA). **(i-j)** Cumulative distribution mEPSC amplitude **(i)** and frequency **(j)**. **(k)** PPR of stimulated EPSCs in CA1 pyramidal neurons. Upper panel: example traces of PPR (inter stimulus interval of 50ms) for 138-floxed (orange) and 138-sponge^{ub} (blue); scale bar: 100 pA, 20 ms. Lower panel: PPRs for different interstimulus intervals ranging from 25 ms to 100 ms (138-floxed vs. 138-sponge^{ub} [mean ± s.d.]: 25 ms, 1.6 ± 0.1 vs. 1.5 ± 0.2 [n=13]; 50 ms: 1.6 ± 0.2 vs. 1.5 ± 0.2 [n=13]; 75 ms: 1.4 ± 0.1 vs. 1.3 ± 0.1 [n=11]; 100 ms: 1.3 ± 0.1 vs. 1.3 ± 0.1 [n=11]. n.s. p=0.14, 0.19, 0.34 and 0.30 for 25, 50, 75 and 100 ms inter stimulus intervals, respectively. Student's two-tailed heteroscedastic t test.)

887 **Supplementary Figure 2**

888 **(a)** Cumulative distribution plots of log_2-fold expression changes (138-sponge^{ub}/138-
889 floxed) for genes either containing 7mer-1a (green), 7mer-m8 (red), 8mer (blue) or no
890 (no site, black curve) predicted miR-138 binding sites. P-value is calculated compared
891 to the no site population and indicated in the graph (KS-test). **(b)** Gene ontology (GO)
892 term analysis for DEGs. Top ten enriched cellular component (CC) GO terms are
893 shown. (C) Expression plots of selected miR-138 binding site containing transcripts in
894 different neuronal subtypes (EXC: excitatory neurons; PV: parvalbumin+ interneurons;
895 SST: somatostatin+ interneurons; VIP: Vasoactive intestinal peptide+ interneurons
896 based on http://research-pub.gene.com/NeuronSubtypeTranscriptomes/. **(d)** Single-
897 molecule FISH analysis of miR-138 (red) together with GFAP antibody stain (green)
898 to label glia cells. Hoechst was used to counterstain nuclei. Arrow points to miR-
899 138/MAP2 positive, GFAP-negative neuron adjacent to glial cell. Scale bar=20 µm. **(e)**
900 Single-molecule FISH analysis of Rims3 mRNA (green) together with Camk2a (grey;
901 left) or Gad2 (grey; right) mRNA to label glutamatergic and GABAergic neurons,
902 respectively. Scale bar=20 µm.
903
904 **Supplementary Figure 3**
905 **(a)** Density of PV+ interneurons in CA1 hippocampus of mice with the indicated
906 genotype. Values are expressed relative to a defined region of interest (ROI). 138-
907 floxed: n=16 ROIs/4 mice; 138-sponge^{PV}: n=18 ROIs/5 mice; data represents the
908 average per mouse ± s.d.; n.s. p=0.55 (Student's two-tailed heteroscedastic t test). **(b)**
909 Percentage of total distance travelled/time spent in the periphery or center of an open
910 field arena during 30 min exploration by mice of the indicated genotypes; 138-floxed
911 n=10; 138-sponge^{PV} n=10; n.s. p=0.38 (Two-way ANOVA). **(c)** Percentage of total
912 time spent in the closed or open arms of an elevated plus maze (EPM) during 5 min
913 exploration by mice of the indicated genotypes; 138-floxed n=10; 138-sponge^{PV} n=10;
914 n.s. p=0.89 (Two-way ANOVA). **(d-f)** mIPSC in CA1 pyramidal neurons. **(d)**
915 Cumulative distribution of mIPSCs frequency. **(e)** Left panel: mIPSC amplitude (138-
916 floxed: range, from 20.9 to 42.5 pA; median, 24.4 pA; IQR, 5.0 pA. 138-sponge^{PV}:
917 range, from 18.0 to 41.6 pA; median, 25.7 pA; IQR, 4.0 pA; n.s. p=0.45 Student's two-
918 tailed heteroscedastic t test). Right panel: cumulative distribution of mIPSCs
919 amplitude. 138-floxed n=22 cells/5mice; 138-sponge^{ub} n=23cells/5mice. **(f)** mIPSC
920 rise (10-90%) and decay (90-10%) time. Left panel: mIPSC rise (10-90%) time (138-

floxed: range, from 1.4 to 2.7 ms; median, 1.9 ms; IQR, 0.4 ms. 138-sponge^{PV}: range, from 1.3 to 2.5 ms; median, 2.0 ms; IQR, 0.4 ms; n.s. p=0.39 Student's two-tailed heteroscedastic t test). Right panel: mIPSC decay (90-10%) time (138-floxed: range, from 9.9 to 13.6 ms; median, 11.1 ms; IQR, 0.9 ms. 138-sponge^{PV}: range, from 9.5 to 14.2 ms; median, 11.6 ms; IQR, 1.8 ms; n.s. p=0.2 Student's two-tailed heteroscedastic t test). 138-floxed n=22 cells/5mice; 138-sponge^{ub} n=23cells/5mice. **(g)** Paired pulse ratio (PPR) of stimulated IPSCs in CA1 pyramidal neurons. Upper panel: example traces of PPR (inter stimulus interval of 100ms) for 138-floxed (orange) and 138-sponge^{ub} (red); scale bar: 100 pA, 50 ms. Lower panel: PPRs for different interstimulus intervals ranging from 50 ms to 150 ms (138-floxed vs. 138-sponge^{PV} [mean ± s.d.]: 50 ms, 0.7 ± 0.2 vs. 0.7 ± 0.1 [n=13]; 100 ms: 0.8 ± 0.1 vs. 0.7 ± 0.1 [n=13]; 150 ms: 0.7 ± 0.1 [n=12] vs. 0.7 ± 0.1. n.s. p=0.46, p=0.44, and p=0.90 for 50 ms, 100 ms and 150 ms, respectively. Student's two-tailed heteroscedastic t test). **(h)** Properties of fast-spiking interneurons. Upper panel: example traces, 138-floxed in orange, 138-songe^{PV} in red, scale bar: 50 mV, 500 ms. Lower panel left: spiking frequency (138-floxed: range, from 123 to 159 Hz; median, 143 Hz; IQR, 29 Hz. 138-sponge^{PV}: range, from 96 to 170 Hz; median, 118 Hz; IQR, 46 Hz; n.s. p=0.31 Student's two-tailed heteroscedastic t test). Lower panel middle: input resistance (138-floxed: range, from 40 to 60 MΩ; median, 57 MΩ; IQR, 18 MΩ. 138-sponge^{PV}: range, from 30 to 71 MΩ; median, 33 MΩ; IQR, 26 MΩ; n.s. p=0.28 Student's two-tailed heteroscedastic t test). Lower panel right: resting membrane potential (138-floxed: range, from -68 mV to -62 mV; median, -64 mV; IQR, 4.5 mV. 138-sponge^{PV}: range, from -70 to -56 mV; median, -67 mV; IQR, 9 mV; n.s. p=0.78 Student's two-tailed heteroscedastic t test). 138-floxed n=5 cells/3mice; 138-sponge^{ub} n=5cells/5mice

Figure 1

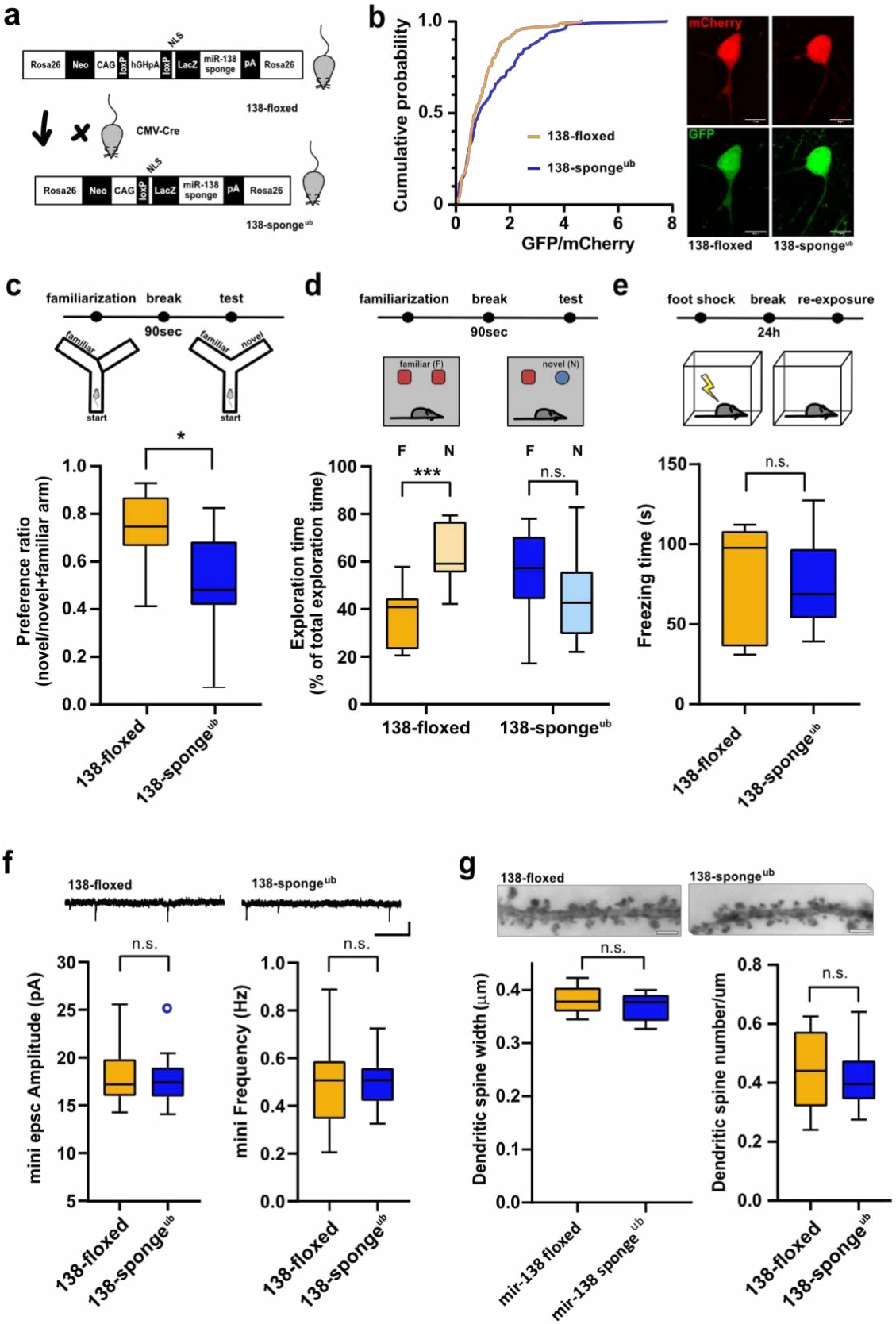

947

Figure 2

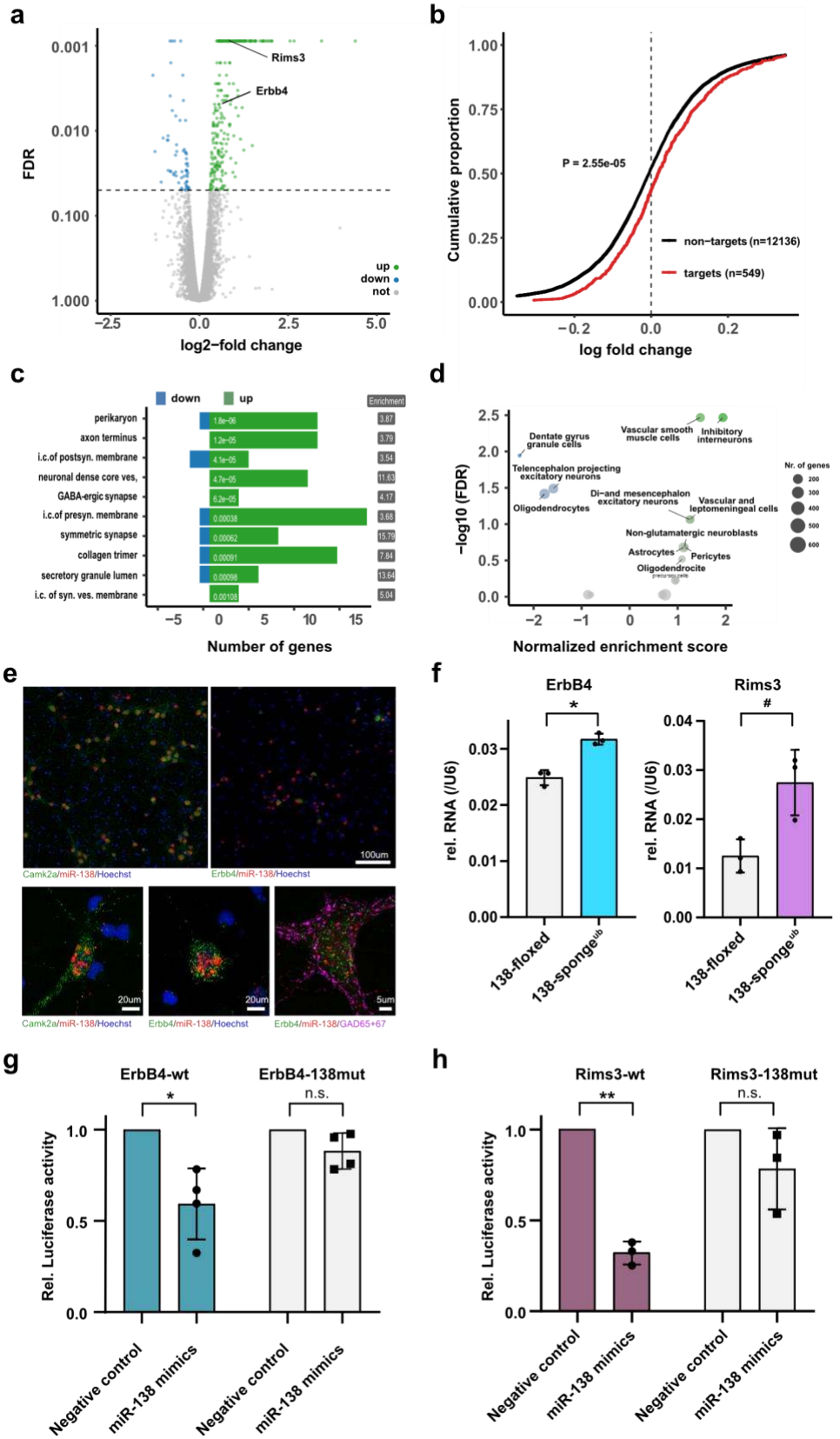

Figure 3

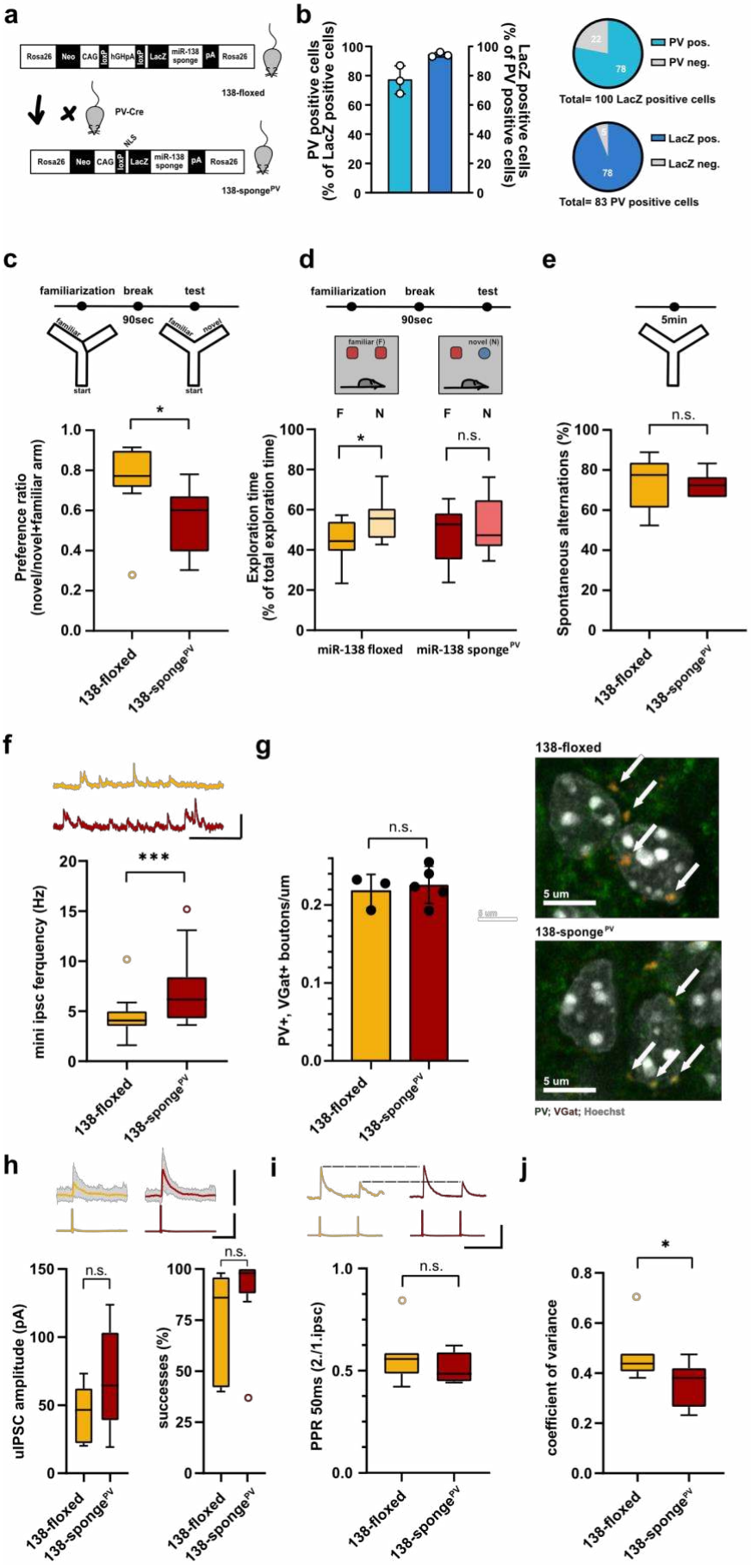

Supplementary Figure1

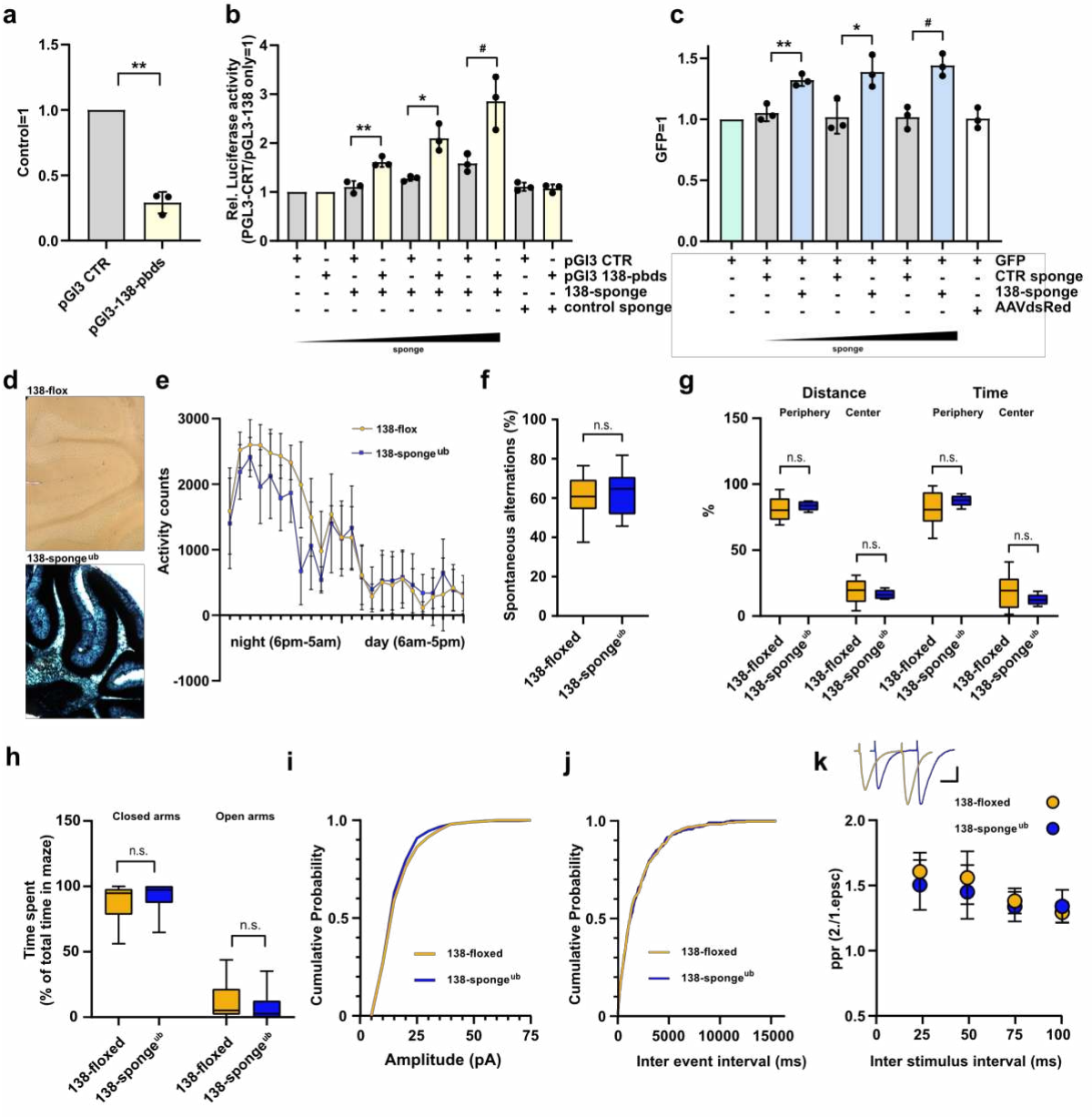

951

Supplementary Figure 2

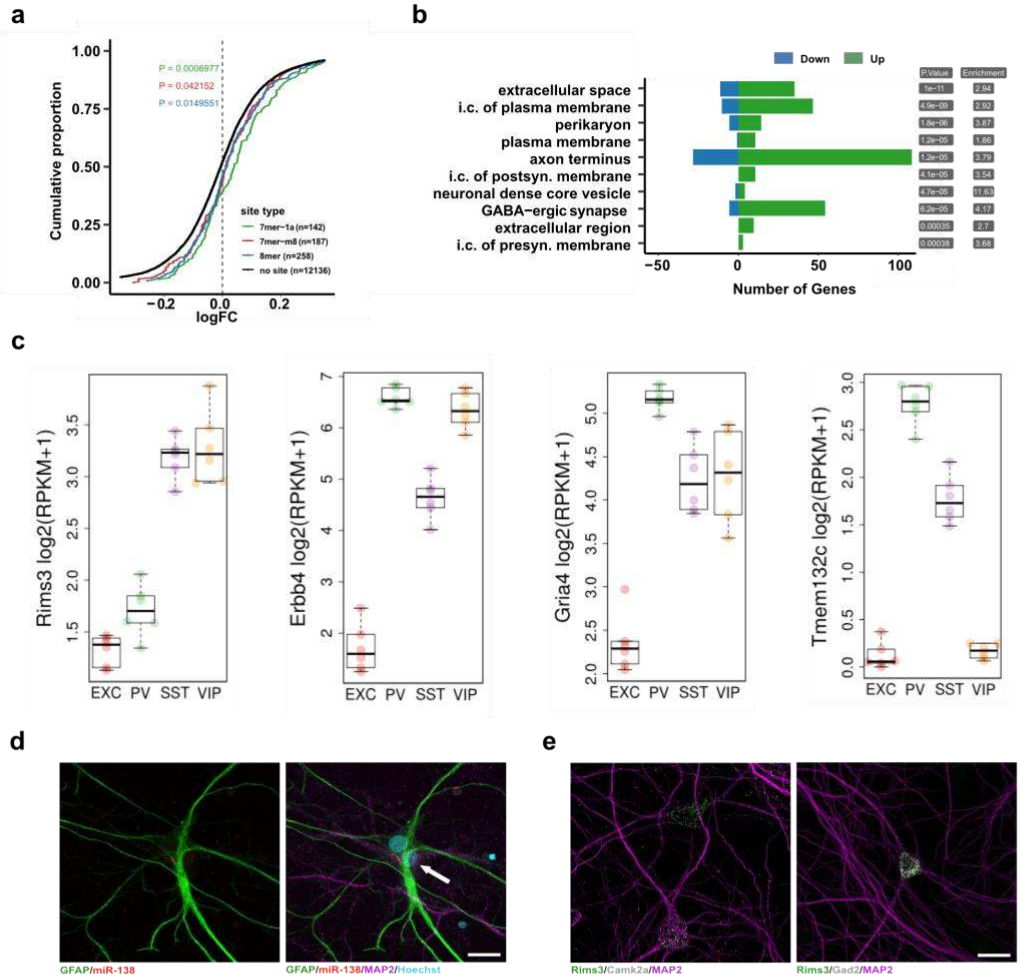

Supplementary Figure 3

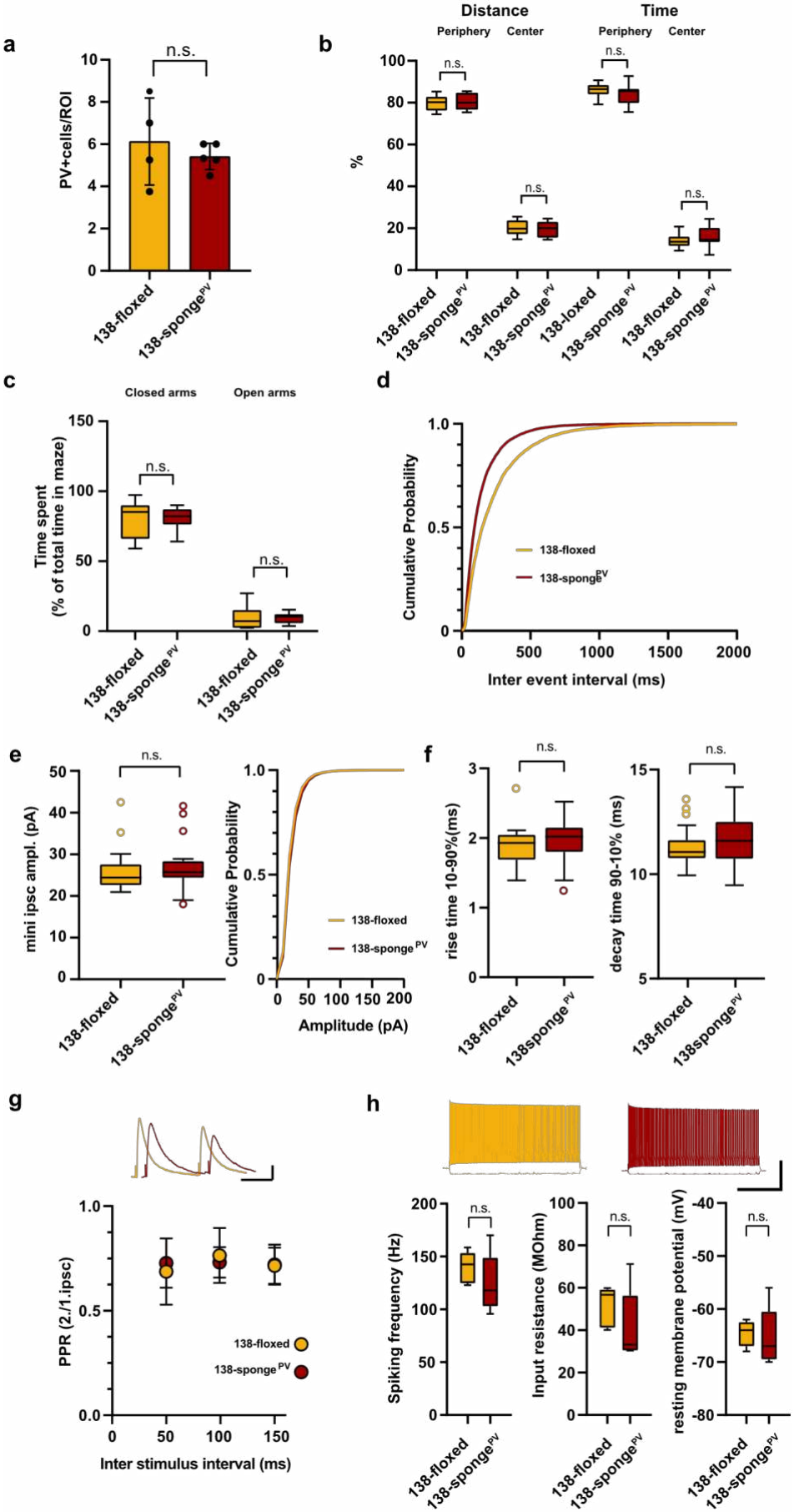

953